PROCEEDINGS OF SPIE

Validation of two techniques for intraoperative hyperspectral human tissue determination

Eric L. Wisotzky, Benjamin Kossack, Florian C. Uecker, Philipp Arens, Steffen Dommerich, et al.

Validation of two techniques for intraoperative hyperspectral human tissue determination

Eric L. Wisotzky[a,b], Benjamin Kossack[a], Florian C. Uecker[c], Philipp Arens[c], Steffen Dommerich[c], Anna Hilsmann[a], and Peter Eisert[a,b]

[a]Fraunhofer Heinrich-Hertz-Institute, Computer Vision and Graphics, Berlin, Germany
[b]Humboldt-Universität zu Berlin, Visual Computing, Berlin, Germany
[c]Charité - Universitätsmedizin Berlin, Department of Otorhinolaryngology, Berlin, Germany

ABSTRACT

Hyperspectral imaging (HSI) is a non-contact optical imaging technique with the potential to serve as an intra-operative computer-aided diagnostic tool. This work analyzes the optical properties of visible structures in the surgical field for automatic tissue categorization. Building an HSI-based computer-aided tissue analysis system requires accurate ground truth and validation of optical soft tissue properties as these show large variability. In this paper, we introduce and validate two different hyperspectral intraoperative imaging setups and their use for the analysis of optical tissue properties. First, we present an improved multispectral filter-wheel setup integrated into a fully digital microscope. Second, we present a novel setup of two hyperspectral snapshot cameras for intraoperative usage. Both setups are operating in the spectral range of 400 nm up to 975 nm. They are calibrated and validated using the same database and calibration set. For validation, a color chart with 18 well-defined color spectra in the visual range is analyzed. Thus, the results acquired with both settings become transferable and comparable to each other as well as between different interventions. Clinical in-vivo data of two different oral and maxillofacial surgical procedures underline the potential of HSI as an intraoperative diagnostic tool and the clinical usability of both setups. Thereby, we demonstrate their feasibility for the in-vivo analysis and differentiation of different human soft tissues.

Keywords: hyperspectral imaging, multispectral imaging, snapshot camera, filter-wheel setup, calibration, human soft tissue, tissue analysis

1. INTRODUCTION

Pathological structures, e.g. tumors, can develop between or in the direct proximity to important structures, e.g. nerves. To reach the operating area, the surgeon has to expose nerves without causing substantial damage.[1] This structure exposition process is of high risk and difficult, because damage to healthy structures, like nerves, can cause a temporary or permanent paralysis of the affected region. Furthermore, in normal light condition, the different pathological tissue types are nearly undifferentiable from healthy neighboring tissue and the detailed anatomy differs widely between each patient. Therefore, it is very time consuming to prepare important tissue without damaging the healthy anatomical structures.[2] This slow and careful process is an important and time consuming part of the operation. An automatic analysis, differentiation and visualization of important tissue structures would allow the surgeon to perform operations faster and with lower risk.

Hyperspectral imaging (HSI) is established in biomedicine for cell segmentation and skin analysis as it shows great potential to derive information about the biophysical and biochemical parameters.[3,4] It has been shown that different tissue types show different optical characteristics in terms of reflection, transmission, and absorption for different wavelengths.[5] Different modalities exist to acquire a hyperspectral data-cube. One possibility is to use different filters in front of the sensor or behind the light source, which sequentially step through the hyperspectral space (filter-wheel setup).[6–8] Such a filter-wheel setup requires time to capture all filter responses

---

Further author information:
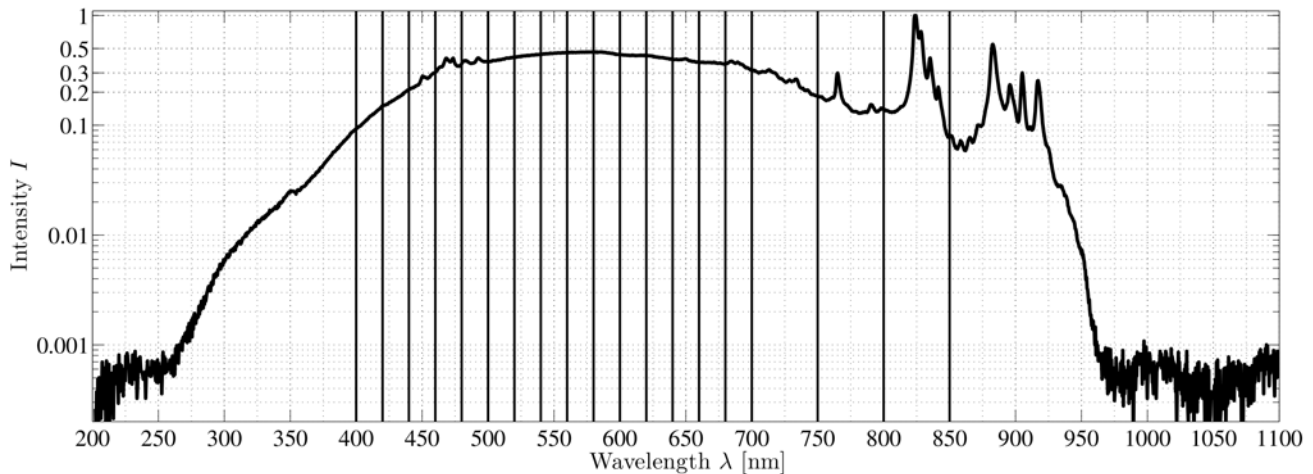E. Wisotzky: E-mail: eric.wisotzky@hhi.fraunhofer.de

Figure 1. The spectrum of the 175 W Xenon light source used in our setup. The relevant interval for illumination is 400 nm to 850 nm. In this interval, specific wavelengths are selected (solid vertical lines for the microscopic filter-wheel setup) for illumination such that the illumination intensity stays constant and intensity peaks (e.g. between 810 nm and 845 nm) are skipped.

and thereby the spectral space. In contrast to the filter-wheel setup, snapshot hyperspectral cameras can be used to acquire the complete data-cube at once, though with lower resolution.[9]

Several HSI systems exist in biomedicine, e.g. hyperspectral snapshot cameras are used in retinal imaging[10, 11] and human cortex imaging[12] as well as filter-wheel setups are used in colorectal tumor imaging.[13] However, HSI has not yet been used for image-guided tissue differentiation.[3, 14] In order to exploit HSI for image-guided tissue differentiation, extensive knowledge about the technical system and the investigated tissue types is important. On one hand, the optical properties of human soft tissue show large variability. On the other hand, the measured raw hyperspectral data cube contains pixel values within each spectral band, which do not necessarily represent the real reflectance of the scanned area. Artifacts of the optics and electronic components influence the measured signals and have to be corrected.[15, 16] Further, as described in Aasen & Bolten,[17] differences in the illumination settings have an influence on the calibration process and the data processing. Finally, the measured signal has to be transformed to a physical system-independent value, e.g. reflectance, to make the data comparable among different settings and useful for signal processing.[18] These aspects make a robust calibration process necessary for potential clinical practice.[19]

This work presents a calibration pipeline for different possible hyperspectral setup configurations addressing the above mentioned challenges. We describe two novel approaches for intraoperative image-guided soft tissue analysis and introduce our robust calibration pipeline, which makes both systems comparable to each other. Both approaches are validated using a color chart with 24 different well-defined spectral tiles[20] as reference spectra. In addition, the resulting data become comparable to data acquired with other spectroscopic analysis methods, e.g. spectrograph. The calibration information provided by the filter and camera manufacturers are validated by analyzing objects with well-known spectrum. Identified variances between measured and reference data are used to adapt the calibration chain for clinical in-vivo analysis. Finally, first clinical results are presented to demonstrate the proposed different optical tissue behavior and to show the feasibility of intraoperative optical tissue differentiation. This is opening the possibility to present additional intraoperative tissue information to the surgeon.

2. METHODS

2.1 Microscopic Filter-Wheel Setup

We build upon the digital microscopic filter-wheel setup presented in Wisotzky et al.[21, 22] and change the illumination unit from a LED source with its challenging inhomogeneous spectrum to a 175 W Xenon (Xe) light

source of LEJ GmbH, Germany. Compared to the previously used LED source, Xe light exhibits an almost homogeneous spectrum in the interesting interval from 400 nm to 850 nm, plotted in Fig. 1. Additionally, the internal DC supply of the Xe source reduces time-based fluctuations of the luminous flux, which allows quantitative long-term microscopic measurements. The luminous flux typically lies at approx. 500 lumen. As this is a low level of intensity, all other light sources, e.g. ceiling and operation light, in the room must be turned off to avoid scattered and indirect light from these sources.

Further, we expand the multispectral range from 16 to 19 channels. To the 16 channels in the visual spectrum (400 nm to 700 nm, with a step size of 20 nm and FWHM of 10 nm), we add three channels in the near infrared (near-IR) spectrum (750 nm, 800 nm and 850 nm). These channels have been chosen because of the wider homogenous spectrum and to avoid the high peak between 800 nm and 850 nm. Each of these three filters has full width at half maximum (FWHM) of 25 nm, see Tab. 1.

The sensor and optics specifications remain the same as presented in Wisotzky et al.[21] The sensor output resolution is 1920×1080 pixels and the used focal length at maximum zoom is 65 mm. The working distance (WD) is about 210 mm.

2.2 Hyperspectral Camera Setup

The alternative hyperspectral imaging (HSI) setup consists of up to two hyperspectral snapshot cameras of XIMEA, Germany. A snapshot camera has the advantage of acquiring the complete hyperspectral dataset in a single shot, while on the other hand the spatial resolution is reduced due to the larger filter array. The first camera holds a 4x4-filter array, resulting in 16 HSI-bands between 460 nm to 630 nm with different FWHM, from $FWHM = 4.69$ nm at 460 nm in band 7 up to $FWHM = 20.18$ nm at 478 nm in band 0, cf. Tab. 1. The second camera holds a 5x5-filter array, sensitive from 600 nm to 975 nm. Since the filters of the camera show two main peak responses in some pixels of the 5x5-filter array, a 675 nm long-pass filter is placed in front of the camera, resulting in 25 HSI-bands between 675 nm to 975 nm with an FWHM range from $FWHM = 3.99$ nm at 693 nm in band 9 up to $FWHM = 25.00$ nm at 955 nm in band 25, cf. Tab. 1. Each band has a specific response pattern containing primary and eventually secondary peaks in the sensitive interval of the sensor, see Fig. 2. Therefore, the band response is not a correct spectral signature as the signal is a combination of the sensor level response and the system level components. To measure a correct spectral signature, it is required to calibrate the signal through spectral correction.[23] Further, the exposure times for both hyperspectral cameras

Table 1. This table shows the spectral peak and FWHM of each band for both setups and all used cameras and filters.

|	Band #	0	1	2	3	4	5	6	7	8	9	10	11	12
Filter-	λ [nm]	400	420	440	460	480	500	520	540	560	580	600	620	640
Wheel	FWHM	10	10	10	10	10	10	10	10	10	10	10	10	10
4x4	λ [nm]	463	471	478	489	490	504	518	531	543	567	580	592	603
Camera	FWHM	10.8	15.5	20.2	10.8	12.1	10.8	9.4	7.4	7.4	7.4	7.4	7.4	10.8
5x5	λ [nm]	693	707	732	746	758	772	784	798	809	821	839	851	861
Camera	FWHM	4.0	4.4	5.1	4.7	7.1	6.8	6.8	8.5	6.8	7.1	10.1	8.1	8.5
	Band #	13	14	15	16	17	18	19	20	21	22	23	24	
Filter-	λ [nm]	660	680	700	750	800	850							
Wheel	FWHM	10	10	10	25	25	25							
4x4	λ [nm]	616	626	638										
Camera	FWHM	13.4	15.5	15.5										
5x5	λ [nm]	872	881	891	900	910	924	932	940	948	955	961	966	
Camera	FWHM	8.8	10.9	12.2	15.0	12.9	15.3	14.2	18.7	19.4	25.0	17.7	15.3	
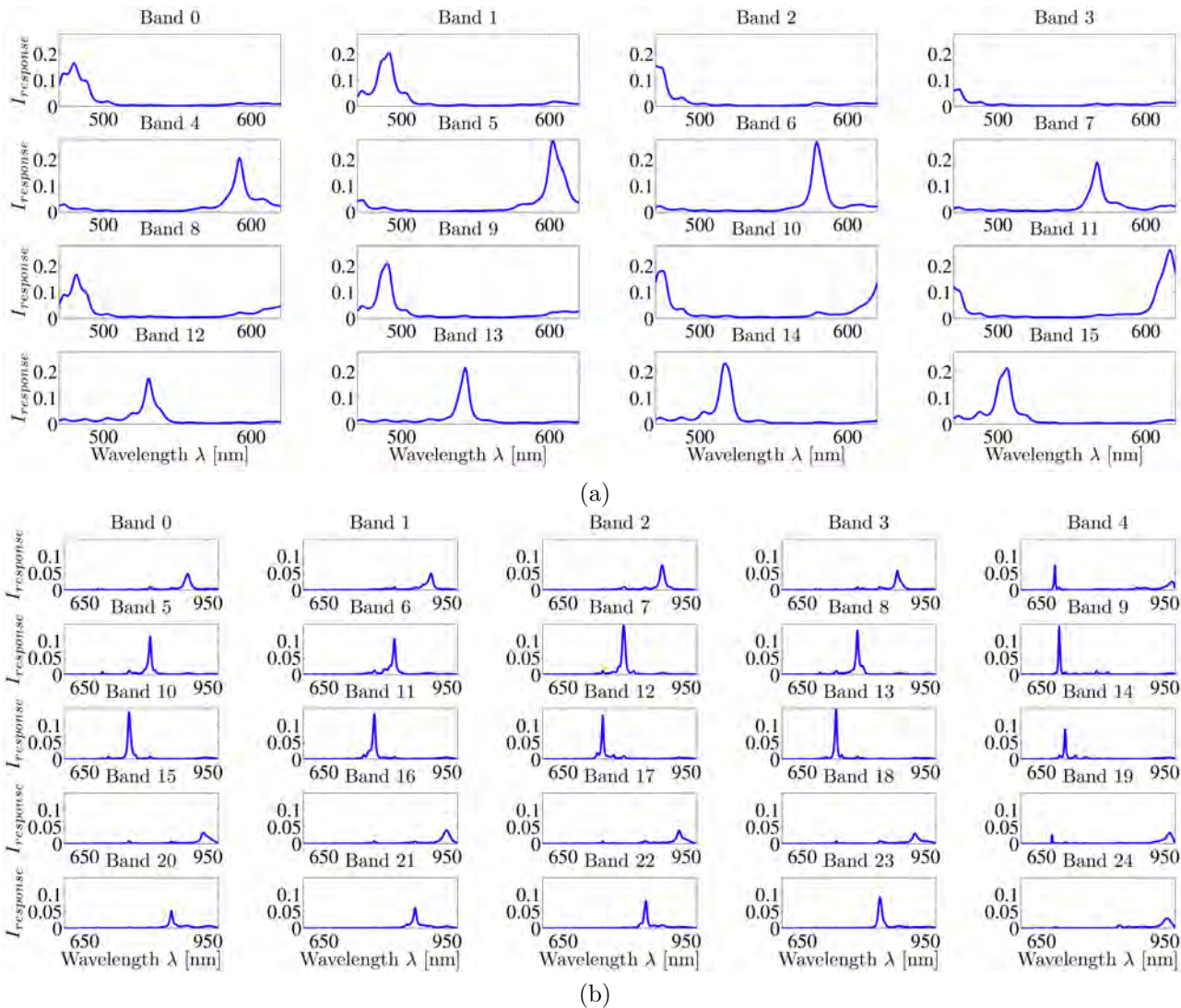
Figure 2. These plots show the specific sensor responses for (a) all 16 band of the 4x4 spectral pattern of the used visual hyperspectral snapshot camera and (b) all 25 bands of the 5x5 spectral pattern of the used near-IR hyperspectral snapshot camera presented by the manufacturer XIMEA, Germany.

will differ due to different sensor response characteristics. For the 4x4 HSI camera, the peak response intensity for each band is about 20%, except band 3 with approx. 10%, see Fig. 2(a). For the 5x5 HSI camera, the peak response intensity for each band is lower with about 10%, see Fig. 2(b). Hence, the exposure time has to be longer for the 5x5 HSI camera to achieve a decent sensor response.

The sensor of both cameras have a resolution of 2048×1088 pixels, at which the filter area is 2048×1024 pixels for the 4x4 HSI camera and 2045×1080 pixels for the 5x5 HSI camera. Both cameras hold a 75 mm f/2.8 lens and are aligned on a rack, focusing on the same point in a distance of approximately 250 mm, which is the working distance of the camera setup. We use two cameras to increase the number of spectral channels over the complete visual and near-IR range (465 nm to 975 nm) while keeping a reasonable resolution. We tested two configurations for scene illumination, the Xe source of the microscopic filter-wheel setup and the surgical LED light.
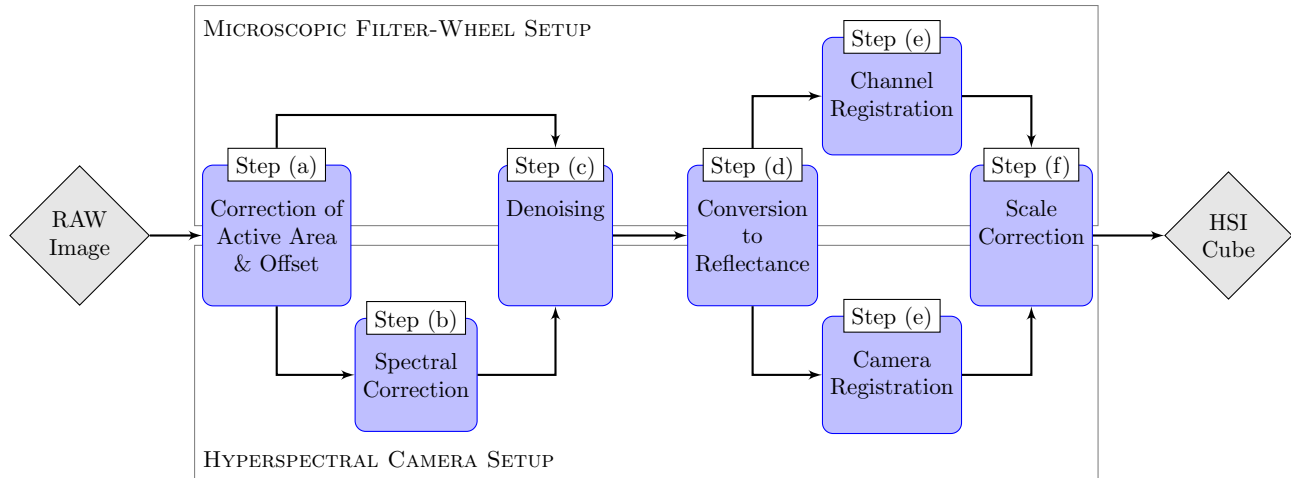
Figure 3. This chart sketches the general calibration workflow for both setups. Calibration step I corrects internal setup artifacts and converts the measurement to reflectance. Step II applies spectral correction and step III is necessary for visualization and validation of the spectral behavior of both setups.

2.3 Calibration Chain

The introduced difficulties and impacts on data quality require a robust calibration with reference data. Since the measurement of the reference data includes uncertainties, errors will propagate into the corrected data, which cannot be quantified in the postprocessing. In order to make the acquired data comparable between the two setups and other spectral acquisition techniques, a joint calibration chain is developed, sketched in Fig. 3. The calibration process has to take the following different aspects into account: a) active area and offset correction, b) spectral correction, c) denoising, d) transforming the measured data to physical units, e) spectral channel registration and f) systematic shift correction.

(a) Active Area and Offset Correction The camera sensor readout of both setups is larger than the active areas. These inactive regions are omitted in the first calibration step. For the HSI cameras, a correct tile order of the mosaic structure is ensured by an offset correction.

(b) Spectral Correction For the hyperspectral camera setup, an additional spectral correction step is needed.[24] A camera specific correction matrix $\mathbf{C}$ is applied to the acquired intensity values I_{raw} to achieve the specific spectral information and to eliminate crosstalks of neighboring pixels

$$I_{cor} = I_{raw} \cdot \mathbf{C}, \qquad (1)$$

where the matrix $\mathbf{C}$ is specifically computed from the available sensor responses (Fig. 2) using pitchfork bifurcation. This matrix $\mathbf{C}$ behaves as a deconvolution of the spectral bands. The corrected signal I_{cor} behaves as if captured with nearly ideal filters. The spectral correction results in 25 channels for the 25 HSI-bands, as only first order peaks of the response pattern are inside the sensitive interval. The 16 HSI-bands result in 27 channels as second order peaks of some band response pattern are inside the sensitive interval, see Fig. 2(a). However, effectively only the 16 first order peaks are used as the second order peaks are noisy and too close to each other. The used spectral channels of both setups are defined in Tab. 1.

(c) Denoising and (d) Conversion to Reflectance The denoising and conversion of raw image data I_{raw} to reflectance I_{res} is achieved in one step including white balance alignment and dark current correction as well. A white reference calibration board (95% reflectance Zenith Lite) is scanned with both setups and all illumination
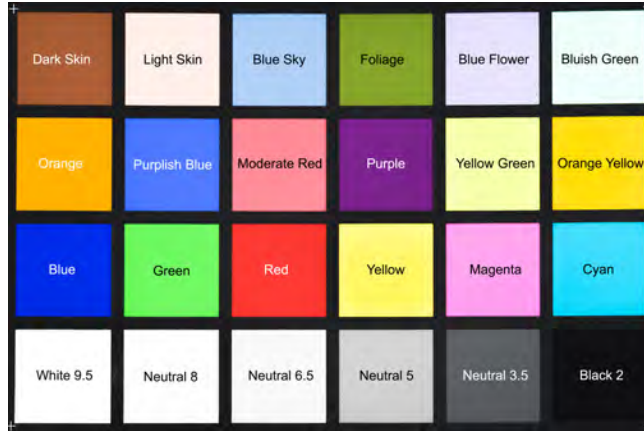
Figure 4. This color chart is used for spectral and scale correction. The 18 colored tiles are used as reference spectra as each color spectrum is well-known. The names of the different colors are written in the corresponding fields to allow comparison of the measured spectra.

settings for the white balance alignment. The achieved intensity I_{white} allows the conversion of raw image data I_{raw} to reflectance I_{res} in a one point calibration method[25]

$$I_{res} = \frac{I_{raw} - I_{dark}}{I_{white} - I_{dark}} \,, \tag{2}$$

where I_{raw} is the measured pixel information (for the HSI camera setup I_{cor} of Eq. 1 is used) and I_{dark} contains the information of a dark reference image (for dark current correction). Artifacts like optical vignetting caused by the used lenses are corrected in this step. For the pixel-wise dark current correction, a series of images with the shielded sensor have been acquired and averaged to I_{dark}, as this increases the signal-to-noise ratio (SNR), defined as

$$SNR = \frac{A_{signal}}{\sigma_{noise}} \,, \tag{3}$$

with the amplitude of the measured signal A_{signal} and the standard deviation of the noise σ_{noise}, of the dark current image. To consider changing conditions, I_{dark} is measured in every measuring sequence using the same setting as the actual acquisitions.

During the calibration, i.e. acquisition of I_{white}, the sensor's view orientation should be the same as during the measurement and the plane of the calibration board should be parallel to the measured surface. Further, shadows on the calibration board should be avoided and the calibration should be carried out with the same optics as used during measurements. In practical application, this is difficult to realize and small errors will be included in this process as specified above.

(e) Channel Registration   To allow building up the hyperspectral data cube for clinical analysis, both acquired images of the 4x4 and 5x5 HSI camera have to be spatially registered. Equally, the sequentially acquired filter-wheel images need to be spatially aligned. This registration process uses normalized cross correlation as cost function to register local specified tissue areas to a hyperspectral data cube.[26]

(f) Scale Correction   Due to uncertainties of the provided calibration information as well as the described internal and external effects, e.g. differences in WD, systematic shifts occure in the reconstructed data for each part in the setups, i.e. filter-wheel setup, 4x4 HSI camera and 5x5 HSI camera. These identified shifts are corrected in the last calibration step using

$$I_{final} = \alpha I_{res} \,, \tag{4}$$

where α is the scaling factor and I_{res} the reflectance intensity from Eq. 2. This scaling factor α is a proportionality constant, which establishes the correlation between spectral illumination intensity and sensor signal response. For constant WD and sensor, it is sufficient to specify α only once.

A chart with 18 colored tiles of well-defined color spectra[20] (see Fig. 4) is scanned with both setups and both illumination options and analyzed to identify α and correct the spectral information assuring an accurate comparison between both approaches. Each color spectrum is known in terms of reflectance, with standard deviation for each data point, in the range of 380 nm and 730 nm with step size of 10 nm. This information is used as reference for the scaling calibration.

The presented calibration chain does not take into account thermal effects or scattered light, thus these need to be avoided as described in Sec. 2.1. To allow comparison of measured clinical data, acquired with both setups, also the magnification has to be comparable. The determination of both field of views is done using a checkerboard, to allow the comparison of the segmentation results.

2.4 First Clinical in-vivo Measurements

To prove both presented approaches in the clinical environment, we have acquired first clinical in-vivo data. The measurement have taken place during two ear-nose-throat (ENT) surgeries. One measurement has been performed during a neck dissection and another during a parotid tumor surgery. In both cases, the surgeon annotated the individual tissue types for later analysis. The regions of different tissue types have been analyzed individually to reconstruct the specific spectral behavior of each type.

3. RESULTS

3.1 Calibration Results

Magnification   The magnification of the camera's field of view differs for both setups. The difference between the filter-wheel and the hyperspectral camera setup is approx. 3:1. The distances between the optics of each setup and the object are identical and in the filter-wheel setup the highest zoom-level is set. This has to be considered during post-processing and tissue behavior analysis, but has no impact on the quantitative results.

Calibration Chain   Fig. 5 substantiate the need of the described calibration chain. It illustrates that acquired pixel values do not represent the actual reflectance information and highly differ between different setups. The comparison of Figs. 5(a) and 5(b) shows only the combination of spectral calibration and conversion to reflection will result in a physically correct spectrum.

For the two different illumination possibilities of the HSI camera setup, the exposure time is longer with Xe illumination, as the luminous flux of the LED surgical light is much higher. The exposure time must be selected such that the full capacity of the sensor sensitivity is optimally used for all bands while a saturation of single bands is avoided. Hence, some channels do not use the full sensor sensitivity and the calculated I_{res} is underestimated. To use the full capacity of the sensor sensitivity, the exposure time for the 4x4 HSI camera is lower compared to the 5x5 HSI camera, resulting in a lower frame rate for the 5x5 HSI camera. This is caused by the differences in the sensor response. A low frame rate has no effect on the calibration results, but has to be considered for clinical measurements. Thus, for the 5x5 HSI camera an exposure time is chosen, which does not use the full sensor sensitivity but keeps an acceptable frame rate. This results in a statistical bias. Therefore, the introduced calibration step (f) scale correction is essential for accurate and comparable signal processing. It will

Table 2. This table shows the identified optimal exposure times for our two setups.

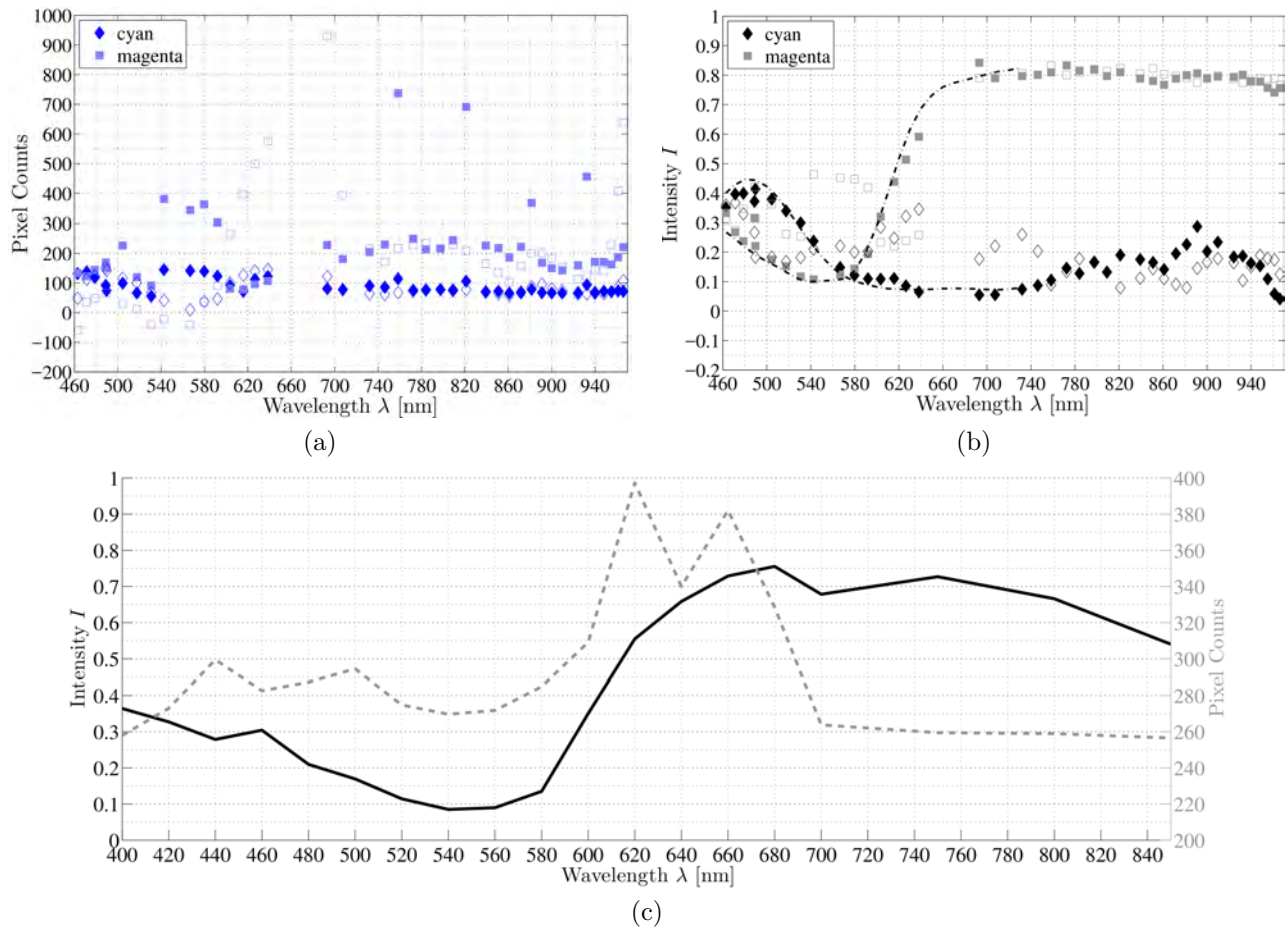| setup	Filter-wheel	4x4 camera	4x4 camera	5x5 camera	5x5 camera
illumination	Xe	Xe	LED	Xe	LED
[ms]	42	65	0.5	110	7.5

Figure 5. These curves substantiate the need of the described calibration chain. The top row, (a) and (b), plots the two reference spectra (□ - magenta tile and ◇ - cyan tile) of the hyperspectral camera setup. The left diagram (a) plots the raw data, the unfilled markers represent the raw sensor counts I_{raw} and the filled markers represent the sensor counts corrected with the specific correction matrix $\mathbf{C}$ from Eq.1. The right diagram (b) plots the corrected data. The unfilled markers represent the calculated reflectance data I_{res} using Eq. 2 without applying Eq. 1 and the filled markers represent the fully corrected data I_{final}, which is the fully corrected physical reflectance. The plot (c) shows the same behavior of the 'magenta' tile for the microscopic filter-wheel. The pixel counts (dotted line) are completely different to the HSI camera setup but the reconstructed spectrum (black line) behaves as the reconstructed line of the HSI camera setup and the reference data.

correct such underestimations as well as differences in WD between the individual cameras using the reference curves. The optimal exposure times identified for our setups and illumination settings are presented in Tab. 2.

The characteristics of the reference color spectra have been correctly reconstructed for all three settings (microscopic filter-wheel setup and hyperspectral camera setup with two illumination possibilities) using the proposed calibration steps (a) to (e). A systematic scale shift is observed in the reconstructed spectral points for

Table 3. This table shows the identified weighting factors α to correct systematic scale shifts of the setup calibration.

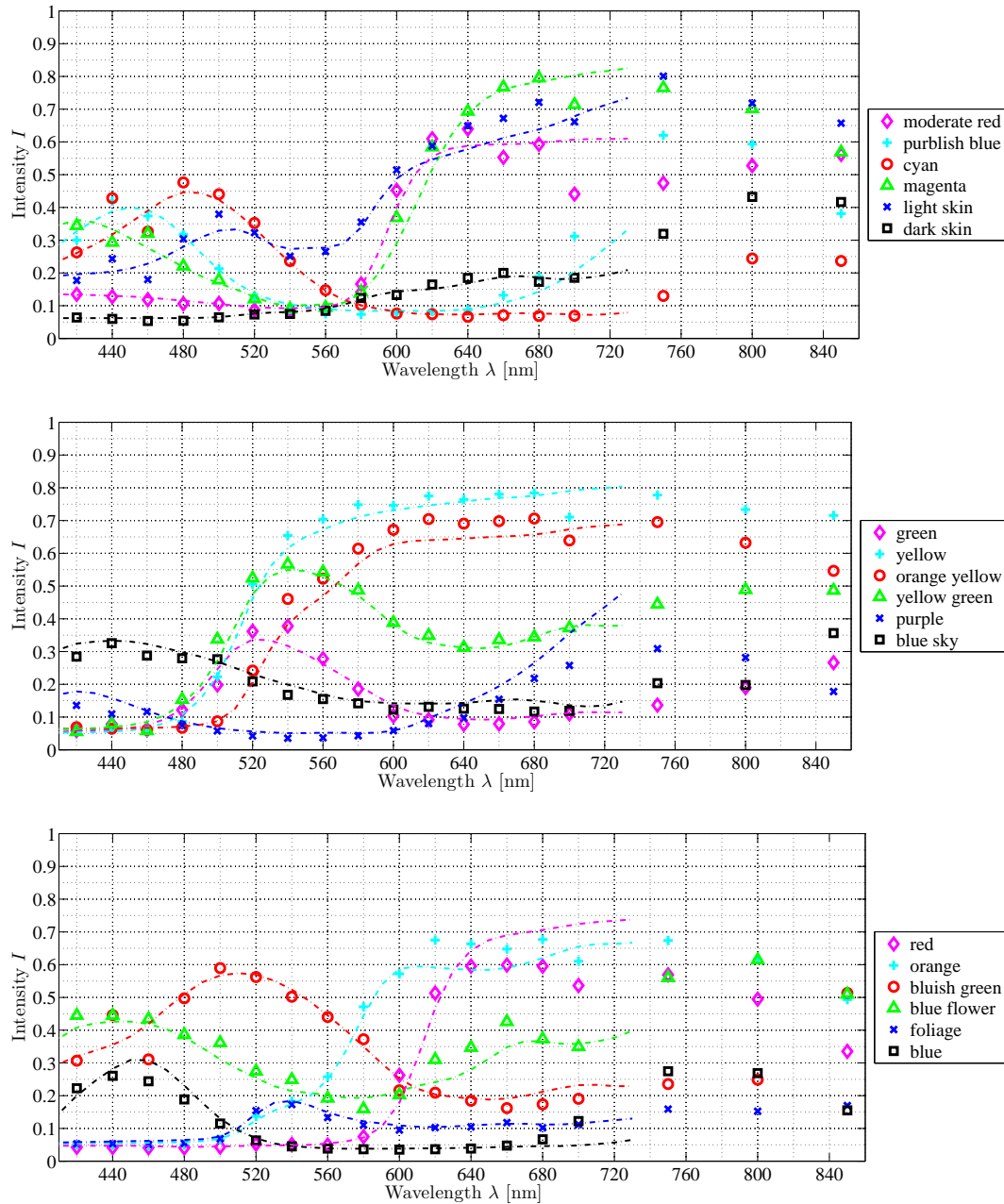| setup	Filter-wheel	5x5 camera	5x5 camera
illumination	Xe	Xe	LED
α	2.0	1.2	0.5

Figure 6. Calibration results of all analyzed color spectra with the filter-wheel setup. The reference data, plotted as dotted lines, could be fully reconstructed for all curves. In the region of near-IR (starting at 730 nm), no reference information are available, but the results are comparable to the results of the hyperspectral camera setup (Figs. 7 and 8).

the microscopic filter-wheel setup and for the 5x5 snapshot camera. Therefore, a weighting factor α is applied, according to the different systematic behaviors of these parts, see Tab. 3. As described, α differs depending on the camera type, the illumination setting and the WD. For the 4x4 HSI camera the internal and external effects, e.g. WD and illumination setting, compensate each other and no significant difference is detected, while for the 5x5 HSI camera and the filter-wheel setup a systematic scale is clearly visible. This is nearly homogeneous for each setting with a growing scale in near-IR. For the Xe illumination setting, the reconstruction overestimates the
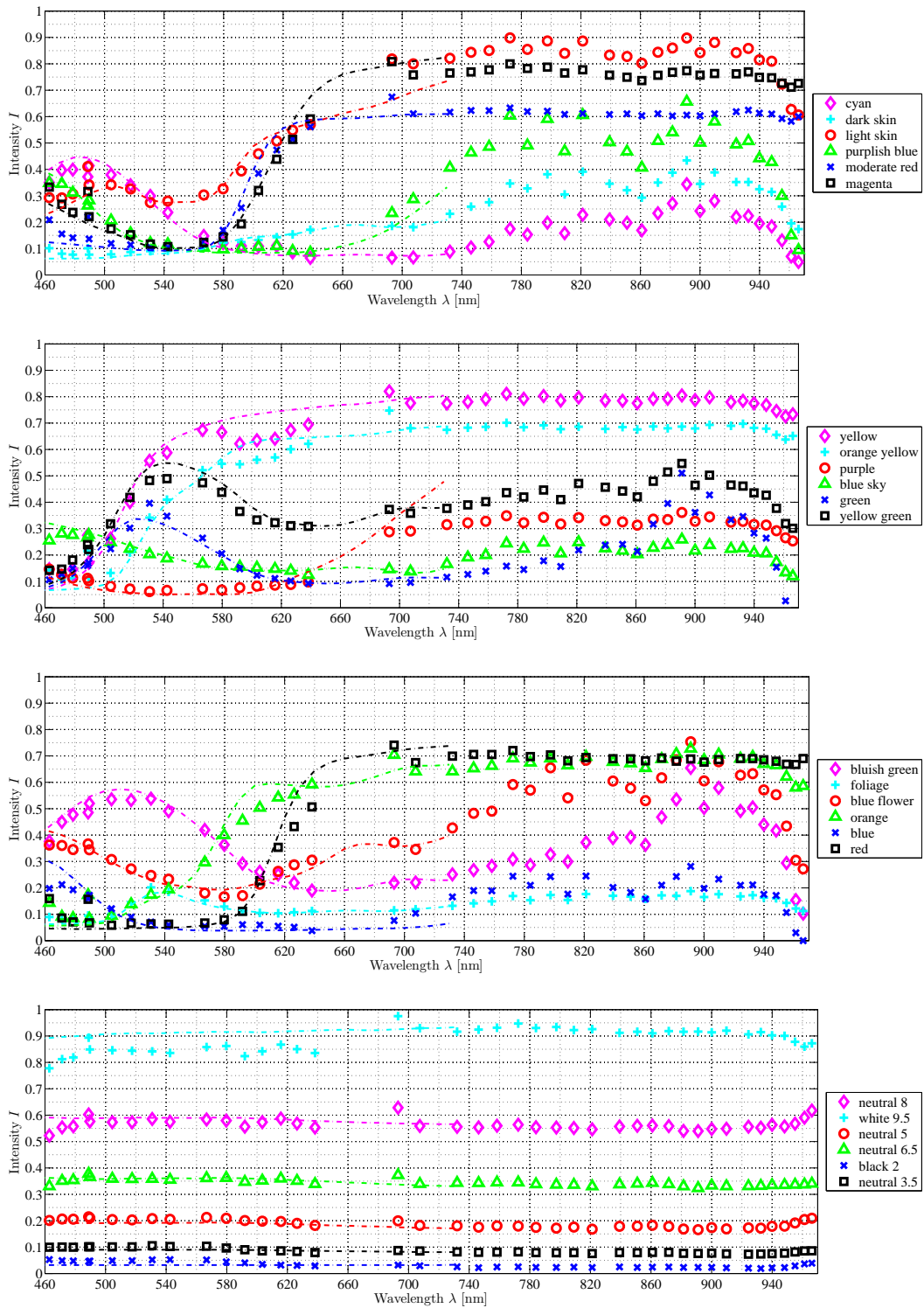
Figure 7. Calibration results of all 24 analyzed color spectra with the hyperspectral snapshot camera setup and Xe illumination. The reference data, plotted as dotted lines, could be fully reconstructed for all curves. In the region of near-IR (starting at 730 nm) no reference information are available, but the results are comparable to the results of the microscopic filter-wheel setup, see Fig. 6.
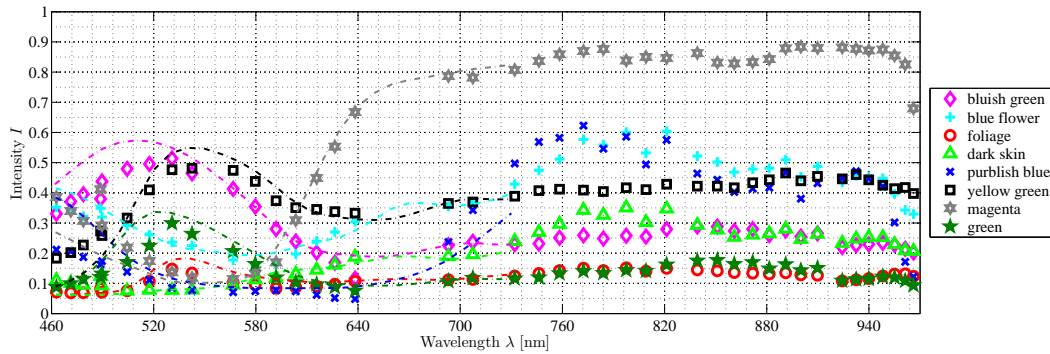
Figure 8. This plot shows a selection of eight out of the 24 measured reference spectra acquired with the hyperspectral camera setup used with LED surgical light. The reference information are plotted as dotted lines. In the region of near-IR (starting at 730 nm) no reference information are available, but the results show the same behavior for all scanned spectra as with the Xe illumination setup.

reference data ($\alpha > 1$), while using LED illumination the reference data are underestimated ($\alpha > 1$). Calibration step (f) corrects these effects.

Fig. 6 plots all 18 reconstructed color spectra, acquired with the filter-wheel setup and corrected with the identified weighting factor α. The data fits to the reference spectra (of the color chart - dotted lines in Figs. 6, 7 and 8) very well. All reference data is within the calculated standard deviations of the reconstructed wavelengths. Beginning at approx. 660 nm, the deviation between reference and calculated intensity is increasing, due to the following reasons: First, the standard deviation (std) of the reference spectra is increasing at about 650 nm. In the visual range, the std is below 1%, while for the red and near-IR spectrum it increases from 2% up to 11%. Secondly, for the near-IR range, the images contain low signal intensities and the SNR is decreasing. This is one reason for underrating the reference data in this range for the 5x5 HSI camera and LED illumination, as this illumination setting offers low intensity in that range. The same effect occurs at 400 nm for the filter-wheel setup.

For the microscopic filter-wheel setup, the SNR in the visual range (420 nm to 680 nm) is $SNR > 3$ and $SNR \approx 2$ at 700 nm, while at 400 nm, 750 nm and 800 nm, it is $SNR \approx 1$ and for 850 nm it is decreasing to $SNR \approx 0.1$.

Fig. 7 shows the 18 reconstructed and corrected color spectra and different gray scales with its respective reference spectrum for the hyperspectral camera setup and Xe illumination. The plots reveal, that the reconstructed data of the 4x4 camera with higher intensity ($I > 0.65$) underestimates the reference values with about 5%. This is caused by the fact that some bands on the sensor do not use the full sensitivity while other bands reach saturation. The same behavior is observed for the 4x4 camera with LED illumination at $I > 0.5$, see Fig. 8. However, all discrepancies between reconstructed and reference intensities are within the permissible error tolerances (measured and stated reference std).

Compared to the filter-wheel setup, the SNR is better at each measured wavelength. For Xe illumination, the average SNR for the visual range (4x4 camera) is $SNR_{avg} = 110.66$ ($SNR_{min} = 11.55$ and $SNR_{max} = 293.99$) and for the near-IR range (5x5 camera) $SNR_{avg} = 0.71$. However, the SNR depends on the chosen exposure time and the used light source. Since the luminous flux of the LED surgical light is much higher compared to the Xe source, the SNR is increased using LED illumination, especially in the near-IR range with an optimal exposure time. For the LED illumination, the average SNR for the visual range is $SNR_{avg} = 151.43$ ($SNR_{min} = 1.28$ and $SNR_{max} = 378.34$) and for the near-IR range $SNR_{avg} = 2.55$.

To compare the three settings, the distances between the reconstructed spectral point to its reference value are calculated for each setting. Fig. 9 shows that the scale correction applied to the filter-wheel setup as well as the 5x5 HSI camera, using the presented α of Tab. 3, reduces the variances from the reference values and makes the data comparable through the settings. The unfilled markers in Fig. 9 show the gap between the reference
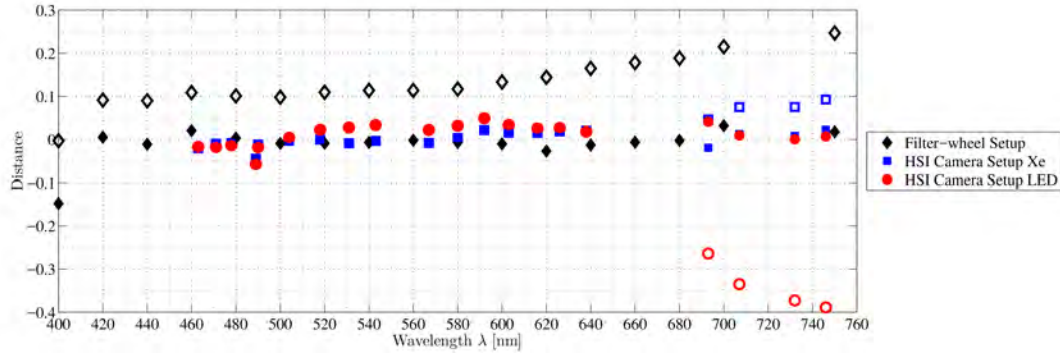
Figure 9. This plot illustrates the quality of the complete calibration chain. The unfilled markers show the calibrated setups without the correction factor α. In this case, the filter-wheel setup shows a systematic shift. Due to the smaller SNR of the near-IR data, the gap between reference and reconstructed data is increasing for all setups. The filled markers show that a correction factor can adjust all settings to the reference and allows comparison among the setup data.
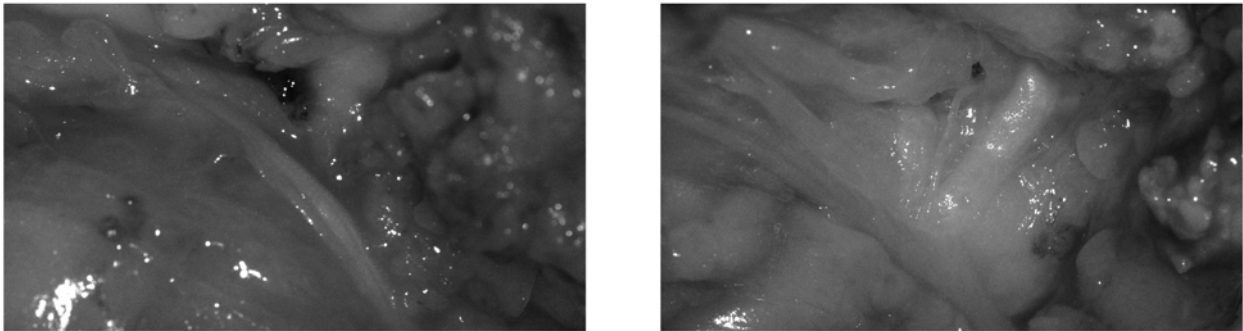

Figure 10. These two images show the two measured views of the two patients at 680 nm with the filter-wheel setup.

data and the reconstructed data using calibration steps (a) to (e), which visualizes the described effect of α for each spectral band.

As all spectra are reconstructed correctly, the results between both setups become transferable and comparable. Thus, the setups can be used for optical tissue analysis, as shown in the next section.

3.2 First Clinical in-vivo Measurements

The first two clinical in-vivo measurements of human soft tissue show different visible behaviors between the various wavelengths for different tissue types. Both setups reveal the same tissue characteristics with respect to internal and external uncertainties. Fig. 10 shows two measured views of two different patients (patient 1 on the left and patient 2 on the right) with the filter-wheel setup, from which the optical behaviors of the nerve and parotid gland tissue are extracted. The spectral curves are presented in Fig. 11. Fig. 12 shows the two camera views with the hyperspectral camera setup (left image: 4x4 HSI camera and right image: 5x5 HSI camera) of patient 1 (cf. 10 left).

After the surgeon annotated the different tissue types in the captured images, binary masks are created to evaluate each type independently. Since a 3D tissue structure is captured, the surface is never perfectly aligned to the camera, and therefore, different tissue types have different orientations to the sensor, the reconstructed optical behavior can differ in a single tissue structure. This results in slightly different spectra for a single tissue type throughout the local regions in a captured view and between several individual patients, see Fig. 11. The curves of one distinct tissue type show the same overall characteristics across different areas for one patient and also across different patients.
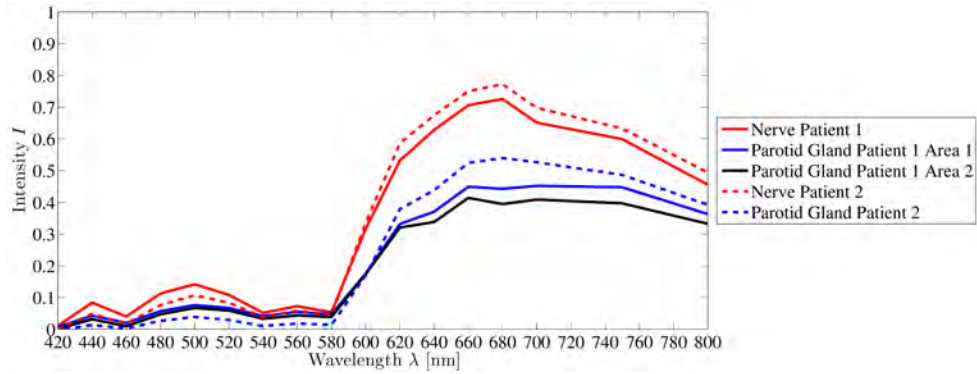
Figure 11. These plots sketch the optical reflectance behavior of nerve and parotid gland of two measured different patients.
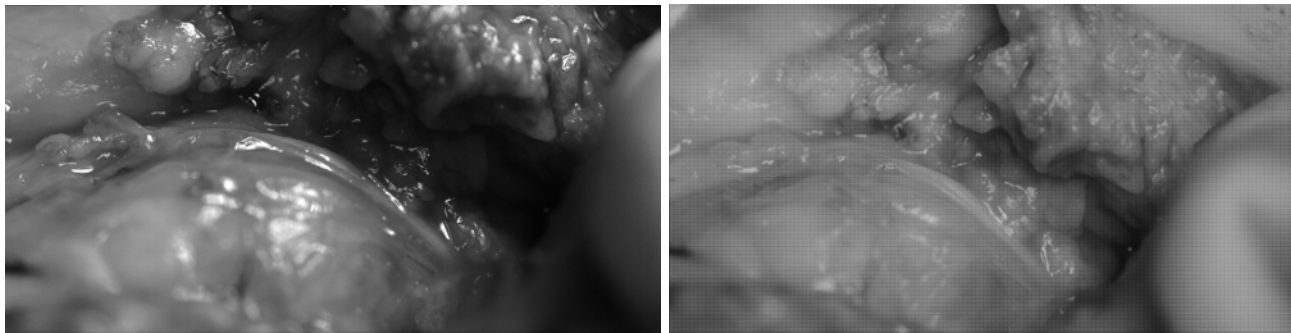

Figure 12. These two views are the same patient as Fig. 10 left but captured with the hyperspectral camera setup. The left image is captured with the hyperspectral 4x4 snapshot camera in the visual range (463 nm up to 638 nm) and on the right, the image from the hyperspectral 5x5 snapshot camera with spectral range from 693 nm to 966 nm is shown.

The optical behaviors differ between different tissue types, as nerves and parotid gland. Nerve reflects with higher intensity in the range of 600 nm up to the near-IR than parotid gland and the specific trends of both tissue types are different over the whole investigated spectrum, especially visible between 620 nm and 700 nm. The same behavior can be observed using the hyperspectral camera setup, see Fig. 13.
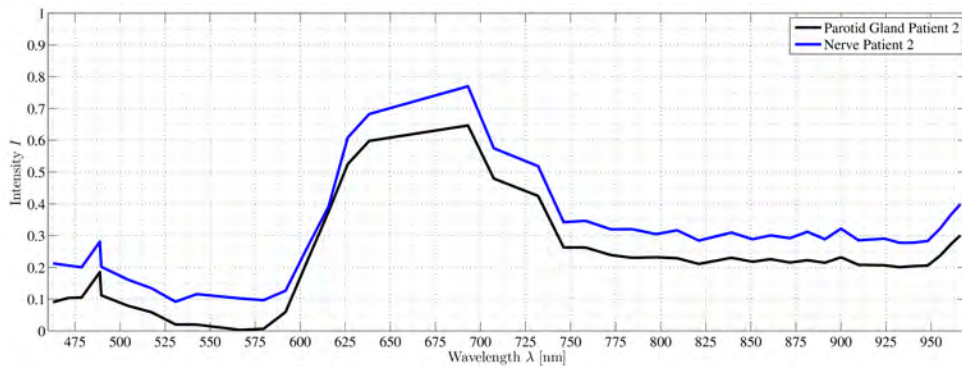

Figure 13. These plots sketch the optical reflectance behavior of nerve and parotid gland of the second patient for the hyperspectral camera setup with surgical LED light.

4. CONCLUSION

In this work, two different hyperspectral setups are presented and calibrated for intraoperative tissue analysis. Both setups allow the same kind of tissue analysis through different approaches. The microscopic filter-wheel setup uses monochromatic illumination of the scene with a camera sensitive over the complete spectral range (400 nm to 850 nm). In the hyperspectral camera setup, the scene is illuminated with white light and separation of the spectral response is done through the sensor setup (with a spectral range of 463 nm up to 966 nm).

The reconstructed reflection data of both setups show the same quality compared with the reference data after using our proposed calibration chain. This allows a comparison of the measured data through the different setups and with other acquisition techniques as spectrometry. Such a robust calibration is essential for soft tissue analysis, as these tissue types show large variability. Further, both setups have been successfully employed in the clinical environment for two different ENT surgeries as at the head region, many important tissue structures are at close range. Based on our calibration and preliminary results, deeper studies of optical tissue behavior, especially human soft tissue, can take place with both setups.

ACKNOWLEDGMENTS

REFERENCES

[1] Wilson, B. C. and Jacques, S. L., "Optical reflectance and transmittance of tissues: principles and applications," *IEEE Journal of Quantum Electronics* **26**(12), 2186–2199 (1990). [doi:10.1109/3.64355].

[2] Jansen-Winkeln, B., Maktabi, M., Takoh, J. P., Rabe, S. M., Barberio, M., Köhler, H., Neumuth, T., Melzer, A., Chalopin, C., and Gockel, I., "Hyperspektral-imaging bei gastrointestinalen anastomosen," *Der Chirurg* **89**, 717–725 (Sep 2018).

[3] Lu, G. and Fei, B., "Medical hyperspectral imaging: a review.," *Journal of Biomedical Optics* **19**(1), 10901 (2014). [doi:10.1117/1.JBO.19.1.010901].

[4] Jacques, S. L., "Optical properties of biological tissues: a review," *Physics in Medicine & Biology* **58**(11), R37–R61 (2013). [doi:10.1088/0031-9155/58/14/5007].

[5] Cheong, W. F., Prahl, S. A., and Welch, A. J., "A review of the optical properties of biological tissues," *IEEE Journal of Quantum Electronics* **26**(12), 2166–2185 (1990). [doi:10.1109/3.64354].

[6] Brauers, J., Schulte, N., and Aach, T., "Multispectral filter-wheel cameras: Geometric distortion model and compensation algorithms," *IEEE Transactions on Image Processing* **17**(12), 2368–2380 (2008). [doi:10.1109/TIP.2008.2006605].

[7] Garini, Y., Young, I. T., and McNamara, G., "Spectral Imaging: Principles and Applications," *Cytometry Part A* **69**(A), 735–747 (2006). [doi:10.1002/cyto.a.20311].

[8] Wisotzky, E., Hilsmann, A., and Eisert, P., "A multispectral method to analyze optical in vivo tissue characteristics," *Medical Physics* **44**(6), 3019 (2017).

[9] Geelen, B., Blanch, C., Gonzalez, P., Tack, N., and Lambrechts, A., "A tiny VIS-NIR snapshot multispectral camera," in [*Advanced Fabrication Technologies for Micro/Nano Optics Photonics VIII*], *Proc. SPIE* **9374**, 937414–1 (2015). [doi:10.1117/12.2077583].

[10] Kaluzny, J., Li, H., Liu, W., Nesper, P., Park, J., Zhang, H. F., and Fawzi, A. A., "Bayer filter snapshot hyperspectral fundus camera for human retinal imaging," *Current Eye Research* **42**(4), 629–635 (2017).

[11] Li, H., Liu, W., Dong, B., Kaluzny, J. V., Fawzi, A. A., and Zhang, H. F., "Snapshot hyperspectral retinal imaging using compact spectral resolving detector array," *Journal of Biophotonics* **10**(6-7), 830–839 (2017).

[12] Pichette, J., Laurence, A., Angulo, L., Lesage, F., Bouthillier, A., Nguyen, D. K., and Leblond, F., "Intraoperative video-rate hemodynamic response assessment in human cortex using snapshot hyperspectral optical imaging," *Neurophotonics* **3**(4), 045003 (2016).

[13] Han, Z., Zhang, A., Wang, X., Sun, Z., Wang, M. D., and Xie, T., "In vivo use of hyperspectral imaging to develop a noncontact endoscopic diagnosis support system for malignant colorectal tumors," *Journal of Biomedical Optics* **21**(1), 016001 (2016).

[14] Calin, M. A., Parasca, S. V., Savastru, D., and Manea, D., "Hyperspectral imaging in the medical field: Present and future," *Applied Spectroscopy Reviews* **49**(6), 435–447 (2014).

[15] Aasen, H., Burkart, A., Bolten, A., and Bareth, G., "Generating 3d hyperspectral information with lightweight uav snapshot cameras for vegetation monitoring: From camera calibration to quality assurance," *ISPRS Journal of Photogrammetry and Remote Sensing* **108**, 245–259 (2015). [doi:10.1016/j.isprsjprs.2015.08.002].

[16] Pichette, J., Goossens, T., Vunckx, K., and Lambrechts, A., "Hyperspectral calibration method for cmos-based hyperspectral sensors," in [*Photonic Instrumentation Engineering IV*], **10110**, 10110, International Society for Optics and Photonics (2017).

[17] Aasen, H. and Bolten, A., "Multi-temporal high-resolution imaging spectroscopy with hyperspectral 2d imagers from theory to application," *Remote Sensing of Environment* **205**, 374–389 (2018). [doi:10.1016/j.rse.2017.10.043].

[18] Burger, J. and Geladi, P., "Hyperspectral nir image regression part i: calibration and correction," *Journal of Chemometrics: A Journal of the Chemometrics Society* **19**(5-7), 355–363 (2005).

[19] Zuzak, K. J., Schaeberle, M. D., Lewis, E. N., and Levin, I. W., "Visible reflectance hyperspectral imaging: characterization of a noninvasive, in vivo system for determining tissue perfusion," *Analytical Chemistry* **74**(9), 2021–2028 (2002).

[20] McCamy, C. S., Marcus, H., Davidson, J., et al., "A color-rendition chart," *Journal of Applied Photographic Engineering* **2**(3), 95–99 (1976).

[21] Wisotzky, E. L., Uecker, F. C., Arens, P., Dommerich, S., Hilsmann, A., and Eisert, P., "Intraoperative hyperspectral determination of human tissue properties," *Journal of Biomedical Optics* **23**(9), 091409 (2018). [10.1117/1.JBO.23.9.091409].

[22] Wisotzky, E., Arens, P., Uecker, F. C., Hilsmann, A., and Eisert, P., "A hyperspectral method to analyze optical tissue characteristics in vivo," *International Journal of Computer Assisted Radiology and Surgery* **13**, S46–S47 (Jun 2018).

[23] Wang, P., Turcatel, G., Arnesano, C., Warburton, D., Fraser, S. E., and Cutrale, F., "Fiber pattern removal and image reconstruction method for snapshot mosaic hyperspectral endoscopic images," *Biomedical optics express* **9**(2), 780–790 (2018).

[24] Khanna, R., Sa, I., Nieto, J., and Siegwart, R., "On field radiometric calibration for multispectral cameras," in [*2017 IEEE International Conference on Robotics and Automation (ICRA)*], 6503–6509 (May 2017).

[25] Polder, G., van der Heijden, G. W., Keizer, L. P., and Young, I. T., "Calibration and characterisation of imaging spectrographs," *Journal of near Infrared Spectroscopy* **11**(3), 193–210 (2003).

[26] Wisotzky, E., Fast, M. F., Oelfke, U., and Nill, S., "Automated marker tracking using noisy X-ray images degraded by the treatment beam," *Zeitschrift für Medizinische Physik* **25**(2), 123–134 (2015). [doi:10.1016/j.zemedi.2014.08.006].